

# NGC 1300 Dynamics:

## I. The gravitational potential as a tool for detailed stellar dynamics

C. Kalapotharakos,<sup>1\*</sup> P.A. Patsis,<sup>1,2,3</sup> and P. Grosbøl<sup>3\*†</sup>

<sup>1</sup>Research Center for Astronomy, Academy of Athens, Soranou Efessiou 4, GR-115 27, Athens, Greece

<sup>2</sup>Observatoire Astronomique de Strasbourg, 11 rue de l'Université, 67000 Strasbourg, France

<sup>3</sup>European Southern Observatory, Karl-Schwarzschild-Str. 2, 85748 Garching, Germany

Accepted .....Received .....in original form .....

### ABSTRACT

In a series of papers we study the stellar dynamics of the grand design barred-spiral galaxy NGC 1300. In the first paper of this series we estimate the gravitational potential and we give it in a form suitable to be used in dynamical studies. The estimation is done directly from near-infrared observations. Since the 3D distribution of the luminous matter is unknown, we construct three different general models for the potential corresponding to three different assumptions for the geometry of the system, representing limiting cases. A pure 2D disc, a cylindrical geometry (thick disc) and a third case, where a spherical geometry is assumed to apply for the major part of the bar. For the potential of the disc component on the galactic plane a Fourier decomposition method is used, that allows us to express it as a sum of trigonometric terms. Both even and odd components are considered, so that the estimated potential accounts also for the observed asymmetries in the morphology. For the amplitudes of the trigonometric terms a smoothed cubic interpolation scheme is used. The total potential in each model may include two additional terms (Plummer spheres) representing a central mass concentration and a dark halo component, respectively. In all examined models, the relative force perturbation points to a strongly nonlinear gravitational field, which ranges from 0.45 to 0.8 of the axisymmetric background with the pure 2D being the most nonlinear one. The force perturbation in each model is found being robust to small changes of the required parameter values. We present the topological distributions of the stable and unstable Lagrangian points as a function of the pattern speed ( $\Omega_p$ ). The topological distribution found deviates in several cases from the classical paradigm with two stable Lagrangian points at the sides of the bar and two unstable ones close to the ends of the bar. In all three models there is a range of  $\Omega_p$  values, where we find multiple stationary points whose stability affects the overall dynamics of the system.

**Key words:** Galaxies: kinematics and dynamics – Galaxies: spiral – Galaxies: structure

### 1 INTRODUCTION

Grand design galaxies are attractive objects for dynamical studies, because it is believed that behind their coherent global features are hidden the basic dynamical mechanisms that shape the morphology of galactic discs. Then, deviations from the grand design could be considered to reflect additional complications of this basic dynamical behavior. The result would be more complicated morphologies, like those encountered in multi-armed or flocculent spiral galaxies. The motivation of this study is to investigate the dynamics of NGC 1300, which is a well known barred-spiral grand design

galaxy with a prominent bar. Its archetypical morphology promises a deeper understanding of the dynamics of a class of similar objects.

Barred-spiral systems offer many examples of grand design morphology, being characterized by a set of two spiral arms starting close to the ends of the bar. In some cases the spirals seem to emerge out of the bar as its continuation, while in others the beginning of the spirals is clearly displaced from the bar's ends (e.g. compare the spirals of NGC 4535 and NGC 4548 in figure 5 in Grosbøl 2008). Nevertheless the morphology of the arms in many of these barred-spiral systems is not as smooth as that of the arms of normal spiral galaxies (Grosbøl & Patsis 1998), especially in near-infrared wavelengths. This can be characteristically seen by overplotting the  $m = 2$  component of the surface brightness on images of galaxies, as do e.g. Seigar et al. (2005). One can observe that their arms are in general asymmetric and have gaps. It is also clear

\* ckalapot@phys.uoa.gr (CK); patsis@academyofathens.gr (PAP); pgrosbol@eso.org (PG)

† Based on observations collected at the European Southern Observatory, Chile: program: ESO 69.A-0021.

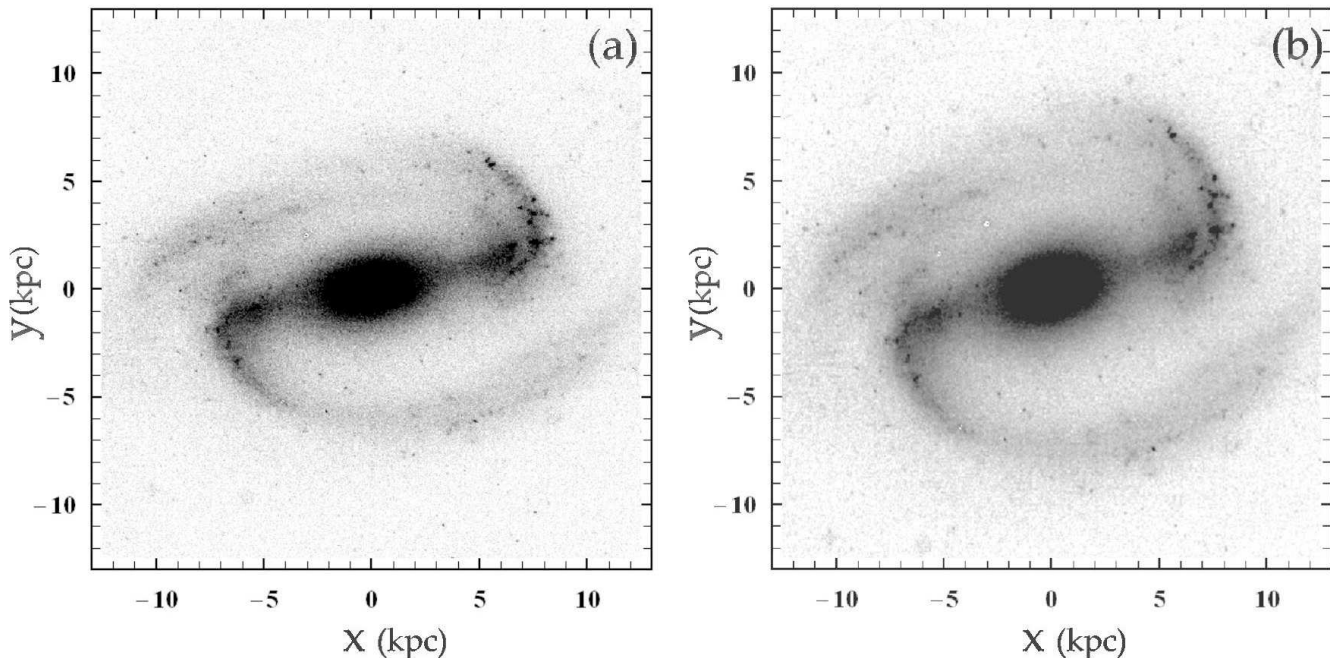


**Figure 1.** (a) The observed K band image of NGC 1300. (b) The deprojected K band image of NGC 1300 using  $(PA, IA)=(87^\circ, 35^\circ)$ . The galaxy was observed with SOFI at the 3.5 m NTT telescope at ESO La Silla. The units on the axes are in kpc, assuming a distance to the galaxy  $D = 19.6$  Mpc. The images are in linear intensity scale.

that in many cases the surface brightness of the arms is larger close to the ends of the bar than at azimuths away from them. Characteristic cases are NGC 4314 and NGC 4665 (Gaddoti 2008). In the case of NGC 4314, in near-infrared wavelengths, the arms hardly complete azimuthally a  $\pi/2$  angle (Quillen et al. 1994).

In the last years the dynamics of barred-spiral systems have been revisited by several research groups. The reason is the investigation of the possibility that the stars on the spirals are in chaotic motion (see also articles by the same authors in Contopoulos & Patsis 2008, and references therein). The motivation for this series of papers is exactly to test this hypothesis in one of the well known and well studied galaxies of this type, NGC 1300. The first step is to estimate its potential directly from observations (de Vaucouleurs et al. 1991). Since it is a well studied object, one can find observations from X-rays to radio wavelengths in order to understand the detailed morphology (e.g. Fabbiano et al. 1988; England 1989). The composite color image STScI-PRC2005-01 (<http://heritage.stsci.edu/2005/01/supplemental.html>), highlights the characteristic asymmetry between the two sides of the galaxy.

Images in optical wavelengths, as well as B–I color maps that cover an area of radius  $\approx 6'$  from the centre of the galaxy, reveal faint extensions of the main bisymmetric spiral structure (e.g. Elmegreen et al. 1996). These extensions, more clearly observed in bluer bands, consist of Population I objects.

In Fig. 1a we present the K band image of the galaxy, that we used in the present study. Images at near-infrared wavelengths depict the morphology of the old disc stellar population and are appropriate for dynamical studies (see Sect. 2 below). The axes

labels are in kpc, assuming a distance to the galaxy  $D = 19.6$  Mpc. At this distance  $1'' \approx 0.095$  kpc.

Our ultimate goal is to present dynamical mechanisms for the stellar component that lead to the development of the particular morphological features of the galaxy NGC 1300. The estimation of a suitable potential is the basis for all dynamical studies and this is done in the present paper, which is structured as follows: In Section 2, we present the observations we performed in order to obtain a reliable estimation of the potential of the galaxy. In Section 3 we describe the image processing techniques that allowed us to create images that will be used to compare our models with. The estimation of the potential is given in Section 4. The forcing in the models is presented in Section 5, while the properties of the corresponding effective potentials in Section 6. Finally we discuss our conclusions in Section 7.

## 2 OBSERVATIONS

The distribution of luminous matter in a galaxy is indicated by its surface brightness map. The translation from luminosity to mass, through a mass-to-light ratio ( $M/L$ ), may vary significant depending on both the spectral band used and the underlying stellar population. The near-infrared K band at  $2.2 \mu$  is close to the emission peak of the old stellar disc and bulge populations which represent the major visual mass constituency of a spiral galaxy (Rix & Rieke 1993). Although very young stars and red super giants also contribute to the K band flux, it remains a good indicator of the mass distribution of luminous matter outside star forming regions.

The K-map of NGC 1300 was observed on 2002-09-01 with SOFI at the 3.5 m NTT telescope, ESO La Silla. The total exposure time on target was 10 min in the  $K_s$  filter, at  $2.162\mu$ , with equal time for sky fields. A jitter pattern with  $10''$  shifts was used to allow removal of bad pixels through stacking, while sky frames were interleaved with offsets around  $10'$  from the galaxy. The SOFI instrument had a Rowckwell Hg:Cd:Te  $1024 \times 1024$  detector with  $0.29''$  pixels on the sky. The field covered the main spiral structure of NGC 1300 but did not provide an accurate estimate of the sky background level. The final K band frame had a seeing of  $0.8''$  and reached a surface brightness of  $K = 20.8 \text{ mag arcsec}^{-2}$  at a signal-to-noise (S/N) level of 3. Thus, the quality of our dedicated SOFI/NTT observations can be considered as an additional advantage for potential calculations, besides the known advantages of the K-band for studies related with the mass distribution in galaxies. For comparison, the 2MASS survey offers a seeing of  $2-3''$  and the corresponding images reach  $20 \text{ mag arcsec}^{-2}$  at a S/N level of  $1\sigma$  (see pages under <http://www.ipac.caltech.edu/2mass/>). The reduction of the SOFI data followed the procedure described by Grosbøl et al. (2004).

The sky projection parameters were adopted from Lindblad et al. (1997) who estimated the Position (PA) and Inclination Angle (IA) by fitting tilted ring models to their HI velocity data. The parameters values they found were (PA, IA) =  $(87^\circ, 35^\circ)$ . These values are different from those one finds by fitting an exponential disc to the regions outside the main bar in the K band image, as in Grosbøl et al. (2004), which are (PA, IA) =  $(106.6^\circ, 42.2^\circ)$ . This values are close to those found by Laurikainen & Salo (2002). However, since for barred spirals like NGC 1300, any determination of the sky projection based on surface photometry may be strongly biased due to the strong  $m = 2$  mode and the open spiral structure, we preferred to use for our study the values proposed by Lindblad et al. (1997). A disadvantage of the use of the near-infrared image is that one can hardly detect the axisymmetric disc in the outer regions. We have to note though, that for the response models and the orbital analysis, we investigated also the effect of the deprojection parameters in the potential, and the results are presented in the forthcoming papers of this series.

The deprojected with parameters (PA, IA) =  $(87^\circ, 35^\circ)$  image of NGC 1300, is shown in Fig. 1b and depicts the morphology we will try to model. The size of this image is  $531 \times 531$  since it has been re-binned to  $0.5''$  pixel size. The standard background subtraction for the K-band frame could be slightly in error since it was based on separate sky exposures and not on the frame itself which was almost fully occupied by the galaxy.

### 3 DATA REDUCTION

We adopted as distance of the galaxy the value  $D = 19.6 \text{ Mpc}$ , according to the cosmology-corrected luminosity distance given in the NASA/IPAC Extragalactic Database (NED). This value may differ from the distance used in other papers on the dynamics of NGC 1300. In any case, the exact distance of a galaxy does not influence essentially the dynamical phenomena that shape its morphology (Patsis et al. 1991).

Before the K-band frame can be used to bootstrap the estimate of the potential, two possible corrections should be considered namely the population effect on the ( $M/L$ ) ratio and the exact background level. Although the major fraction of flux in the K-band originates from the old stellar, disc population (Rix & Rieke

1993), young stars in the arm regions will bias the effective  $M/L$ . The young stellar population may be present both as a diffuse, unresolved, component and as resolved young stellar complexes seen in the arms as bright knots (Patsis et al. 2001; Grosbøl & Dottori 2008). In order to reduce the  $M/L$  bias from young stars, we removed such bright knots by a digital filter. A correction that has to be done concerns the brightness of the outer parts of the galactic disc. This area is biased towards higher values due to the presence of young stellar clusters and stellar complexes, still present even in K band images (Patsis et al. 2001; Grosbøl & Dottori 2008). For this purpose, in Fig. 1b we firstly removed the bright spots in the region with a radius  $R > 6.5 \text{ kpc}$ . Bright spots, assumed to be young clusters, do not cover areas larger than  $10 \times 10$  pixels. We substituted the intensities of all extreme high (but also a few low) valued pixels with the median value of the corresponding  $961 (31 \times 31)$  pixels area centred at the very pixel under consideration. In Fig. 2a only the identified as high valued pixels are shown, while in Fig. 2b we see the rectified image of the galaxy after the removal of the bright spots. After these reductions the galaxy image seems quite smooth in the area of high valued pixels (Fig. 2b) but still presents significant noise in the area of low valued pixels. In Fig. 2c we see how noisy is the contour corresponding to the brightness value  $20.8 \text{ mag arcsec}^{-2}$ . In order to smooth out the image, we apply a low-pass smoothing filter which affects only the low valued pixels ( $\geq 19 \text{ mag arcsec}^{-2}$ ) getting a less noised image (Fig. 2d).

In Fig. 2d we indicate four radial directions A, A', B and B', centred at the axes origin, along which we plot the surface brightness  $\Sigma(R)$  after applying the smoothing filter. We have chosen the directions along the minor axis (A, A') which reveal better the exponential disc. The directions (B, B') are along the diagonal of the image nearest to the minor axis and provide data for longer distance. The surface brightness along these directions is given in Fig. 3a. It is obvious that no exponential profile is observed at the outer parts of the disc (beyond the region with the bar and spiral structures) as expected. This implies that the adopted zero value level for the background is not correct. Therefore, we decrease the zero value level by the smallest quantity so that the surface brightness profiles become exponential, i.e.

$$\Sigma(R) \propto e^{-R/h_R}, \quad (1)$$

as shown in Fig. 3b (actually we increase the brightness values of all pixels by the same quantity). We consider the region with the spiral arms part of the exponential disc. We note that the applied correction is of the order of the background uncertainty. The corresponding scale length we find in that case is  $h_R \approx 10 \text{ kpc}$ . By increasing the brightness by a smaller value than the one we finally applied, we do not get a well defined exponential profile. The value of  $10 \text{ kpc}$  we find is in agreement with the one given by Prieto et al. (2001) corresponding to observations of NGC 1300 in the I band. We note that Laurikainen & Salo (2002) and Laurikainen et al. (2004) find values close to  $7 \text{ kpc}$  in their 2MASS and H-band images respectively. The effect of such differences on the nonlinearity of models for the potential is investigated below (Sect. 5).

### 4 THE ESTIMATION OF THE POTENTIAL

After all the above amendments we result in an estimation for the surface density distribution of the *luminous* component in the reduced image (Fig. 2b), under the assumption of a constant mass-to-light ratio. In our approach we reconstruct the galactic potential assuming the maximum contribution of the luminous component

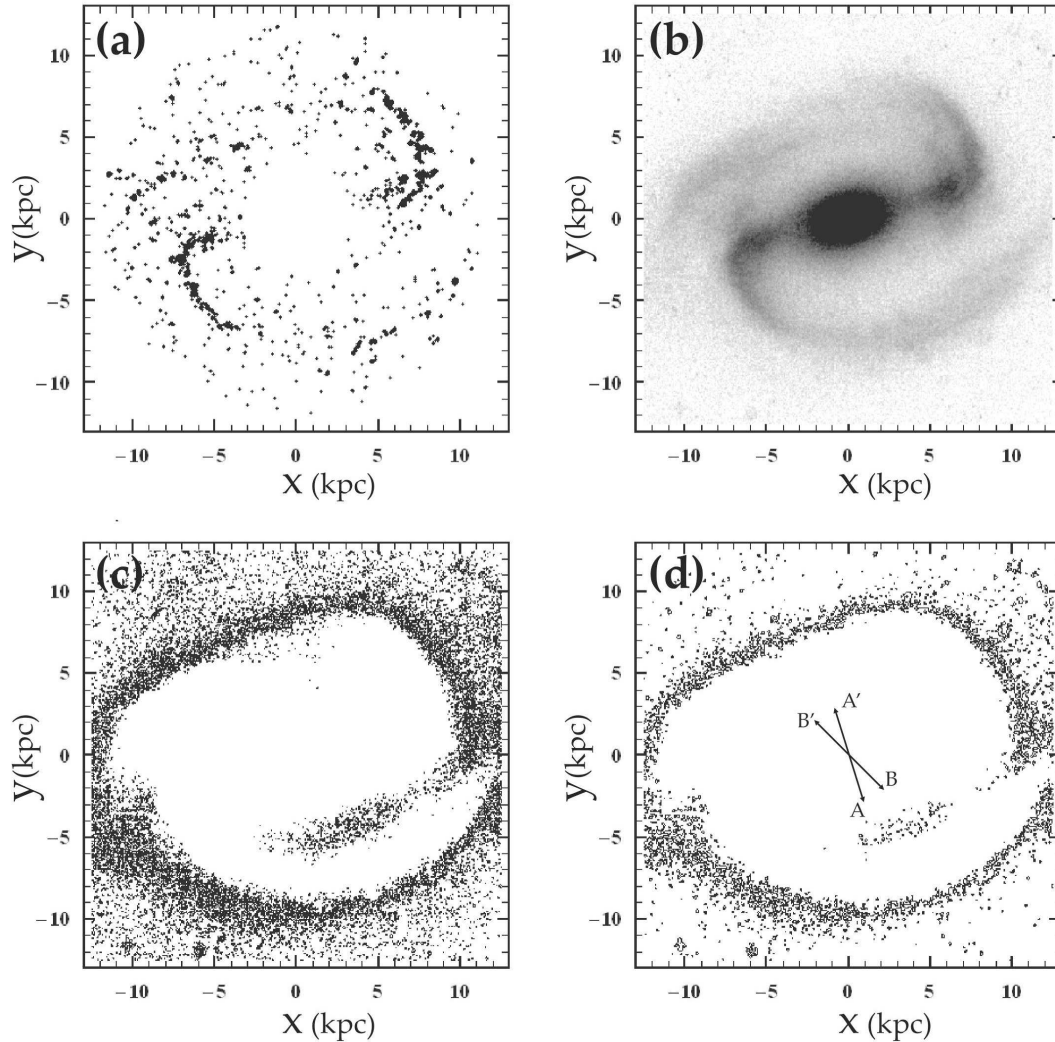


**Figure 2.** (a) The bright spots identified as young clusters. These regions correspond to extreme high valued pixels. (b) The K band image of NGC 1300 after reducing the intensities of the extreme high valued pixels. This image is smoother than the one in Fig. 1b and lacks of bright areas corresponding to young clusters. (c) The contour line for  $20.8 \text{ mag arcsec}^{-2}$  for the image panel (b). It is obvious that the low brightness data are noisy. (d) The same contour line, as in (c), after the application of a low-pass smoothing filter to low brightness pixels ( $\geq 19 \text{ mag arcsec}^{-2}$ ). The arrows A, A', B, B' denote the directions along which we plot the surface brightness in Fig. 3.

**Table 1.** All the parameter values used in (7), (8) and (16) for each model (see text). These values correspond to the rotation curves of the models in Figs. 4, 7 and 5. The last two columns read the total mass inside the (spherical) radius  $r = 15 \text{ kpc}$  for the luminous (LC) and dark (DC) component respectively.

models	$M_{CMC}(M_{\odot})$	$a_{CMC}$ (kpc)	$M_{DH}(M_{\odot})$	$a_{DH}$ (kpc)	$j_0(M_{\odot} \text{ kpc}^{-3})$	$a_{MHP}$ (kpc)	LC ( $M_{\odot}$ )	DC ( $M_{\odot}$ )
Model A	$7.0 \times 10^8$	0.1	$8.0 \times 10^{11}$	30	-	-	$5.0 \times 10^{10}$	$7.6 \times 10^{10}$
Model B	$2.3 \times 10^9$	0.1	$1.6 \times 10^{12}$	40	-	-	$6.5 \times 10^{10}$	$7.5 \times 10^{10}$
Model C	$9.4 \times 10^8$	0.07	$1.6 \times 10^{12}$	40	$6.12 \times 10^{10}$	0.19	$7.1 \times 10^{10}$	$7.5 \times 10^{10}$

to the observed rotation curve as given in Lindblad et al. (1997). For the cases that parts of the rotation curve will not be able to be entirely assigned to the luminous component we switch on two additional components in our modelling. They represent a dark halo and/or a central mass concentration. Since our goal is the study of the dynamics of the stars, treated as test particles moving in the es-

timated gravitational field, the total potential must be compatible with the rotation curve of the galaxy, in every model we study.

In order to proceed with the potential estimation of the luminous component we need to do an assumption about the distribution of the matter in the third dimension. Below, we study three different cases. The basic difference among these three general models

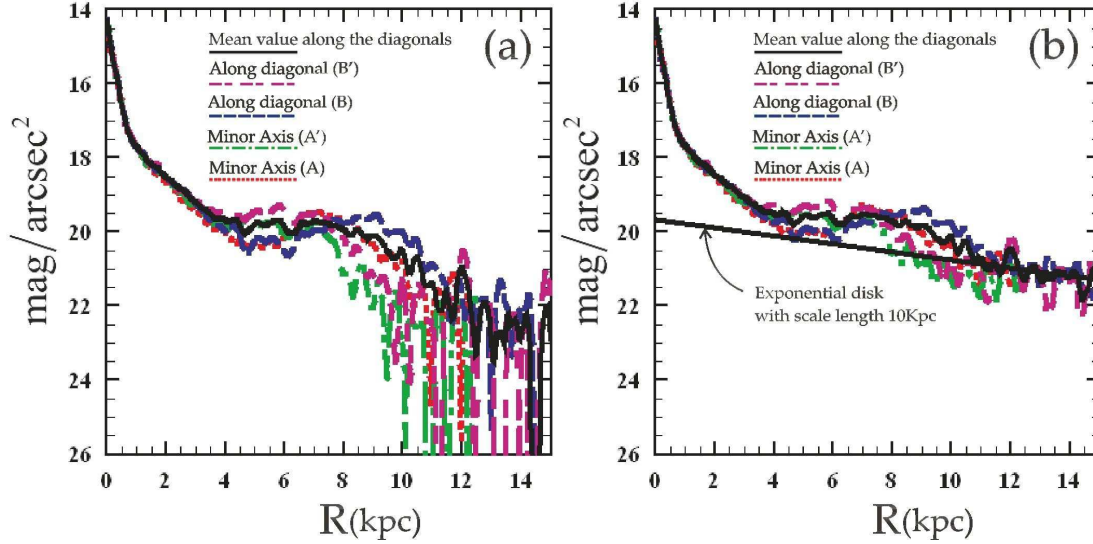


**Figure 3.** (a) The surface brightness along the directions indicated in Fig. 2d. We observe that no exponential law can be identified in the outer parts, which means that the considered zero level is not correct. (b) The surface brightness along the same directions after the minimum correction of the zero level so that an exponential decrement is obtained in the outer parts. The scale length of the resulting exponential law is 10 kpc.

is their *geometry*. We want to compare the marginal thin geometry of the 2D case (model A) with a thick disc case (model B) in order to see if the comparison between galaxy and models improves by varying our parameters towards the one or the other direction in the parameter space. Model C changes essentially the geometry of the bar from cylindrical to a combination of spherical with cylindrical and should be again considered as a limiting case. More specifically we consider:

**Model A.** The ‘2D’ or ‘degenerate’ case in which all matter is considered lying on the  $(x, y)$  galactic plane.

**Model B.** The ‘disc’ case in which we assume a cylindrical geometry and that all matter is distributed in a 3D disc with scale height  $h_z$ . Then the vertical dependence of the density  $\rho$  reads (van der Kruit 1988)

$$\rho \propto \rho_z(z) = \frac{1}{2h_z} \operatorname{sech}^{2/n} \left( \frac{nz}{2h_z} \right), \quad (2)$$

where  $h_z$  is the vertical scale height and  $n$  is an index (see Section 4.2, for its meaning).

**Model C.** The ‘spheroidal’ case in which we consider that the total observed brightness is the combination of two major components: i) a spheroidal component that accounts for the major part of the bar and ii) a 3D exponential disc with scale height  $h_z$  as in model B. The spheroidal component includes the bulge ( $r < 1.5$  kpc, Prieto et al. 2001; Laurikainen & Salo 2002; Laurikainen et al. 2004) and the axisymmetric contribution of the central part of the bar.

In Cartesian coordinates for a given spatial density  $\rho(x, y, z)$  the gravitational potential  $\Phi(x, y, z)$  is

$$\Phi(x, y, z) = -G \int \frac{\rho(x', y', z') dx' dy' dz'}{\sqrt{(x-x')^2 + (y-y')^2 + (z-z')^2}}, \quad (3)$$

where  $G$  is the gravitational constant. This means that  $\Phi(x, y, z)$  is the convolution of the functions  $\rho(x, y, z)$  and  $g(x, y, z) = \frac{1}{r} =$

$\frac{1}{\sqrt{x^2 + y^2 + z^2}}$ . Thus the potential is written as  $\Phi = \rho \otimes g$ , where  $\otimes$  denotes the convolution operator.

#### 4.1 Model A

In model A, where all mass is assumed on the  $(x, y)$  plane, the density can be written as  $\rho(x, y, z) = \Sigma(x, y)\delta(z)$ , where  $\Sigma$  is the surface density and  $\delta$  is the delta function. Substituting the above density expression into (3) and integrating it over  $z$  we get

$$\Phi(x, y, 0) = -G \int \Sigma(x', y') g(x-x', y-y', 0) dx' dy' \quad (4)$$

which is the convolution of the functions  $\Sigma(x, y)$  and  $g(x, y, 0)$ . Knowing the surface density  $\Sigma(x_i, y_j)$  at each grid point  $(i, j)$  we can calculate the potential at the same grid points by using the convolution theorem

$$\Phi = \mathcal{F}^{-1} [\mathcal{F}(\Sigma) \mathcal{F}(g)], \quad (5)$$

where  $\mathcal{F}$  and  $\mathcal{F}^{-1}$ , denote the Fourier transform and inverse Fourier transform respectively. We use an extended square area 16 times larger than the original area of the image of the galaxy in order to avoid the contribution from periodic reflections of the signal from the galaxy’s pixels. Such an extended area will allow us to consider, in dynamical studies, stars that travel to large distances away from the centre of the galaxy. The surface density in the extended area is considered to be zero. We use the 2D fast Fourier transform (FFT) technique for the corresponding computations. Note, that in this calculation the adopted  $g(0, 0, 0)$  value is equal to  $(\text{bin size})^{-1} \approx 21 \text{ kpc}^{-1}$  since the softening length is of the order of the bin size. A detailed description of the whole procedure can be found in Hohl & Hockney (1969).

Given the potential values at the grid points one can calculate the potential everywhere in between these points using a 2D interpolation scheme. However, such a scheme, besides its complexity, provides the potential taking into account non-smooth, local density disturbances. For this reason we proceed as in Quillen et al.

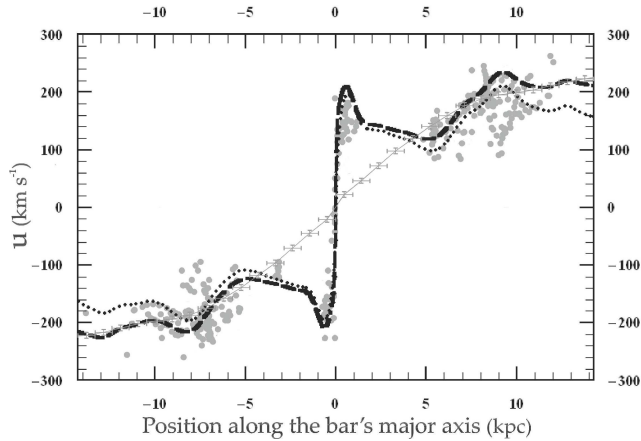


**Figure 4.** The rotation curve of model A together with observational data by Lindblad et al. (1997). Gray dots correspond to optical measurements from various slits aligned close to the major axis of the galaxy. The gray curve with the error bars correspond the HI rotation curve given in Lindblad et al. (1997). The dotted line represents the rotation curve of the luminous component only along the major axis of the bar in model A. The dashed curve is obtained by considering also an additional central mass (CMC) and a dark halo (DH) component. The importance of these terms are determined by the parameters given in Table 1.

(1994) and we decompose the potential into its azimuthal Fourier components at every radius  $R$ . Under this consideration the potential can be written in polar coordinates  $(R, \theta)$  as

$$\Phi(R, \theta) = \Phi_0(R) + \sum_{k=0}^{k_{max}} [\Phi_{kc}(R) \cos(k\theta) + \Phi_{ks}(R) \sin(k\theta)]. \quad (6)$$

For  $k_{max} \rightarrow \infty$  the form (6) returns exactly the same values with those we have from the 2D interpolation scheme mentioned above. We cut off the high harmonics and consider all terms (even and odd) up to  $k_{max} = 6$ . Like this we are able to reproduce all the important morphological features of the galaxy (its asymmetries included). Quillen et al. (1994) calculated the amplitudes  $\Phi_{kc}(R)$ ,  $\Phi_{ks}(R)$  for many rings  $R_i$  and fitted them by 8th order polynomials. Despite the advantages of simplicity and analyticity of the expressions for each function that the use of polynomials secures, it is not capable of following the actual variations well. For this reason in the present study we apply the interpolation scheme with cubic splines to the  $(R_i, \Phi_{kc}(R_i))$ ,  $(R_i, \Phi_{ks}(R_i))$  data sets. This scheme guarantees the continuity of the potential, of the forces and of derivatives of the forces, which are used in the variational equations providing indicators that will measure the chaoticity of the orbits (e.g. Lyapunov exponents). This is particular important for stellar dynamical investigations, which is our motivation for the estimation of the NGC 1300 potential. Note that we set  $\Phi_{kc}(0) = \Phi_{ks}(0) = 0$  in order to secure the continuity required at  $R \rightarrow 0$ . Table 2 in Appendix<sup>1</sup> presents all the amplitude values, at 101 successive radii  $R_i$ , used for the derivation of the interpolating splines.

Figure 4 shows the HI rotation curve (gray solid line with error bars) together with optical velocity measurements (gray dots) from various slits aligned close to the major axis of the galaxy, as taken from Lindblad et al. (1997). In this figure we have also plotted a rotation curve along the major axis of the bar, corresponding to the potential (6) of the luminous matter only (dotted line). In this

case it has been considered being  $5.0 \times 10^{10} M_\odot$  (see Table 1). This curve fails reproducing the flat part of the rotation curve at large distances. This implies that some additional mass component exists besides the luminous component. The most reasonable candidate to be invoked is a dark halo (DH) term. As already mentioned our general model foresees the switching on of two additional components for a central mass concentration (CMC) and a DH. We model both of them with a Plummer sphere since it is simple, effective and widely used in the literature. The importance of these terms are controlled by the parameters of the Plummer spheres. Thus the total potential  $\Phi_T(R, \theta)$  can then be written

$$\Phi_T(R, \theta) = \Phi_{LM}(R, \theta) + \Phi_{CMC}(R) + \Phi_{DH}(R) \quad (7)$$

where  $\Phi_{LM}$  is the luminous matter component given by (6) and

$$\Phi_{DH}^{CMC}(R) = -\frac{GM_{DH}^{CMC}}{\sqrt{R^2 + a_{DH}^{CMC}{}^2}}, \quad (8)$$

is the potential for the Plummer spheres, with  $a$  being a constant parameter. The adopted parameters are given in Table 1 (Model A). In Fig. 5 we see that the DH term is quite important and helps the rotation curve of the model reaching the level of the HI curve of Lindblad et al. (1997). On the other hand the CMC term is less important increasing the central peak by  $\approx 12$ km/sec which eventually reaches the value  $\approx 208$ km/sec. Note that the central peak value is not well defined by the observational data and therefore the adopted parameter values for the CMC term provide only a reasonable area in the parameter space.

## 4.2 Model B

In case B we assume that the density can be written as

$$\rho(x, y, z) = \Sigma(x, y)\rho_z(z). \quad (9)$$

van der Kruit (1988) proposed a family of models regarding the vertical dependence of the density which reads

$$\rho_z(z) = A \operatorname{sech}^{2/n} \left( \frac{nz}{2h_z} \right) \quad \text{with } n \in [1, \infty), \quad (10)$$

where the normalization constant  $A$  is given as

$$A = \frac{\Gamma\left(\frac{1}{2} + \frac{1}{n}\right)}{2h_z \sqrt{\pi} \Gamma\left(1 + \frac{1}{n}\right)}, \quad (11)$$

so that  $\int_{-\infty}^{\infty} \rho_z(z) dz = 1$ .  $\Gamma$  is the Gamma function defined by

$$\Gamma(w) = \int_0^{\infty} t^{w-1} e^{-t} dt. \quad (12)$$

Varying  $n$  from  $n = 1$  to  $n \rightarrow \infty$  we get  $\rho_z(z)$  varying from

$$\rho_z(z) \propto \operatorname{sech}^2 \left( \frac{z}{2h_z} \right)$$

(isothermal disc) to

$$\rho_z(z) \propto \exp \left( -\frac{|z|}{h_z} \right)$$

(exponential disc). de Grijs (1998) and Kregel et al. (2002) provide estimations for the mean values of the parameter  $n$  and the ratio  $h_R/h_z$  in samples of galaxies, which are  $n \approx 3.7 \pm 0.6$  and  $h_R/h_z \approx 7.3 \pm 2.2$ , respectively (for a review see van der Kruit 2002). These studies have been based on observations in I and K bands.

We adopted the values  $n = 4$ ,  $h_R/h_z = 7$ , which give

<sup>1</sup> Appendix is only available in electronic form



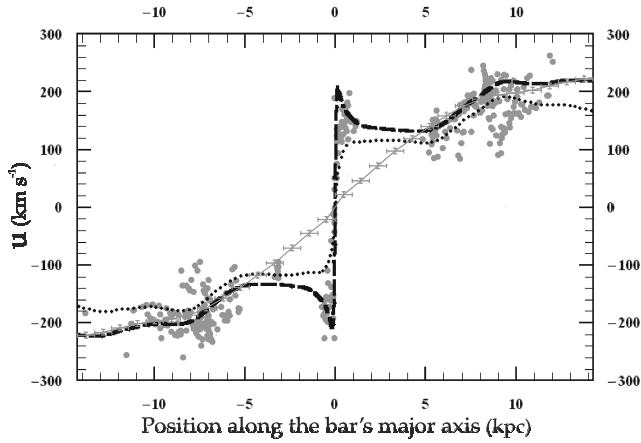


**Figure 5.** The rotation curve along the major axis of the bar for model B. The drawn curves are as in Fig. 4. We observe that the luminous component alone (dotted curve) reaches lower velocity values at the central and outer parts of the galaxy with respect to the velocity measurements. The added CMC component is  $\approx 3$  times more massive than in case A. The rotation curve corresponding to the total potential (7) with the parameter values shown in Table 1 levels off at about the same  $u_{max}$  as the HI rotation curve. Note that the central peak is sharper in this case.

$h_z \approx 1.43$  kpc and following Quillen et al. (1994), we substitute the density expression (9) into (3) and by integrating over  $z$  we obtain

$$\Phi(x, y, 0) = -G \int \Sigma(x', y') g_B(x - x', y - y') dx' dy', \quad (13)$$

where the function  $g_B$  is given by

$$g_B(x, y) = \int_{-\infty}^{\infty} \frac{\rho_z(z') dz'}{\sqrt{x^2 + y^2 + z'^2}}. \quad (14)$$

Thus, the potential  $\Phi$  on the galactic plane is the convolution of the functions  $\Sigma$  and  $g_B$ . We can again calculate it applying the convolution theorem  $\Phi = \mathcal{F}^{-1} [\mathcal{F}(\Sigma) \mathcal{F}(g_B)]$ , since we know the surface density  $\Sigma(x_i, y_j)$  at every grid point  $(i, j)$ .

We note that Laurikainen & Salo (2002) and Laurikainen et al. (2004) introduced an improved version of the Quillen et al (1994) method, where the image pixels are first smoothed by calculating the azimuthal Fourier decompositions of the surface density in different radial zones in polar coordinates. This approach has some advantages, like a possibility to use more noisy images and to apply radially non-constant vertical models. However, for high quality images and for strongly barred galaxies (like our data for NGC 1300) the differences in the resulting potential should be negligible regardless of the integration method.

Working in the same way as in model A we obtain expressions mathematically similar to (6) for the potential corresponding to the luminous component and to (7) for the total potential. Table 3 in Appendix contains all the values of the amplitudes for  $\Phi_0(R_i)$ ,  $\Phi_{kc}(R_i)$ ,  $\Phi_{ks}(R_i)$  calculated for 101 rings at  $R_i$ . The specific values for  $\Phi_0$ ,  $\Phi_{kc}$ ,  $\Phi_{ks}$  correspond to  $6.5 \times 10^{10} M_\odot$  for the mass of the luminous matter.

Finally, Fig. 5 presents the rotation curve corresponding to model B together with the observational data (Lindblad et al. 1997) as we did in Fig. 4 for the 2D case. The dotted line gives the rotation curve along the major axis of the bar when we take into account only the luminous component. We observe that this rotation curve reaches lower values than the observational one also at the central parts. For this reason we add a CMC term which is  $\approx 3$

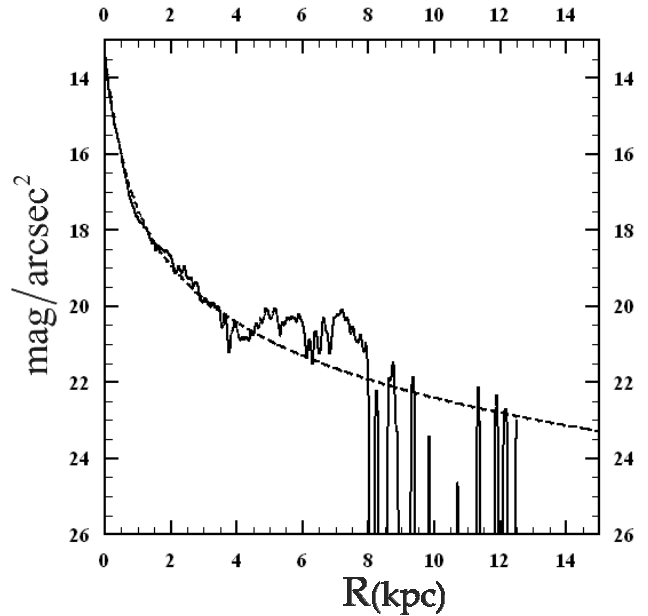


**Figure 6.** The surface brightness of the MHP term in model C. The solid line represents the mean (over azimuth) surface brightness after the subtraction of the exponential disc surface brightness (see Fig. 3b) from the total one. This part is fitted by the MHP with the parameter values shown in Table 1 (dashed curve).

times more massive than the one we added in model A, i.e. now it is  $2.3 \times 10^9 M_\odot$ . We add also a DH term in order to get a better description at the outer parts of the disc. The dashed line gives the rotation curve of the total potential (7) with the corresponding parameter values given in Table 1.

### 4.3 Model C

In this case we consider that the main part of the bar can be described with a spherical component. This part could be vaguely described as “the bar without its ansae” (Fig. 1b). For this purpose we use the modified Hubble profile (MHP) (see Binney & Tremaine 2008, p. 68)

$$\rho_{MHP} = j_0 \left[ 1 + \left( \frac{r}{a_{MHP}} \right)^2 \right]^{-3/2}. \quad (15)$$

The parameter  $a_{MHP}$  is the scale length and the parameter  $j_0$  determines the mass inside a specific radius (e.g.  $r \leq a_{MHP}$ ). Note that the mass inside a radius, in MHP model, diverges logarithmically at large radii and therefore it is meaningless to refer to total mass. The corresponding potential via Poisson equation is

$$\Phi_{MHP} = -\frac{GM_h(r)}{r} - \frac{4\pi G j_0 a_{MHP}^2}{\sqrt{1 + \left( \frac{r}{a_{MHP}} \right)^2}}, \quad (16)$$

where

$$M_h(r) = 4\pi a_{MHP}^3 j_0 \times \left[ \ln \left( \frac{r}{a_{MHP}} + \sqrt{1 + \left( \frac{r}{a_{MHP}} \right)^2} \right) - \frac{r}{a_{MHP}} \left[ 1 + \left( \frac{r}{a_{MHP}} \right)^2 \right]^{-1/2} \right]. \quad (17)$$

By integrating (15) over  $z$  we take the expression for the sur-

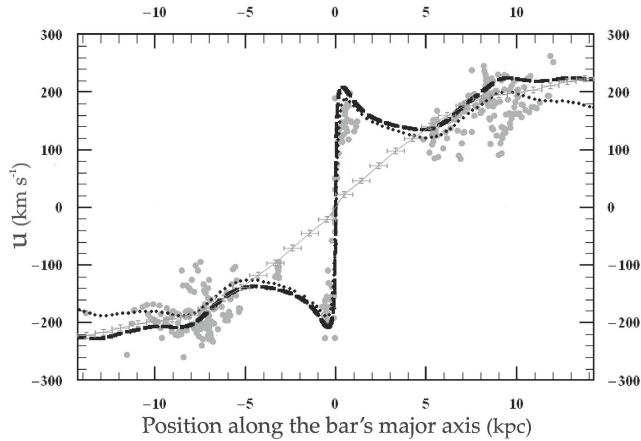


**Figure 7.** Rotation curve together with observed velocities for model C. Drawn curves are as in Figs. 4 and 5. The rotation curve of the luminous matter along the bars' major axis is given with the dotted curve. The corresponding curve of the total potential including CMC and DH components, with the parameter values given in Table 1 is represented by the dashed curve.

face density for MHP, which is

$$\Sigma_{MHP}(R) = \frac{2j_0 a_{MHP}^3}{a_{MHP}^2 + R^2} \quad (18)$$

In order to find the values of the best fitting parameters of the MHP model we subtract the exponential disc  $\Sigma_d \propto e^{-R/h_R}$  with  $h_R=10$  kpc (see Fig. 3b) from the observational surface density  $\Sigma_{obs}$  so that the remaining luminosity at the central region ( $R < 4$  kpc) is mainly due to the assumed spherical component. In Fig. 6 we plot the azimuthally mean surface brightness of the central area of the galaxy (solid line) after the subtraction of the exponential disc. We also give the curve corresponding to (18) (dashed curve) with the parameter values shown in Table 1. We observe that the MHP gives a reasonable fitting of the inner 3.5-4 kpc.

The total potential corresponding to the luminous mass is the sum of the MHP component (16) and the component corresponding to the remaining mass. The surface density of the latter component  $\Sigma_D$  is derived by subtracting the surface density  $\Sigma_{MHP}$  from the surface density  $\Sigma_{obs}$  we derive from the observations. Thus, the surface density (of the remaining disc)  $\Sigma_D(x_i, y_j)$  at each pixel ( $i, j$ ) is given by

$$\Sigma_D(x_i, y_j) = \Sigma_{obs}(x_i, y_j) - \langle \Sigma_{MHP}(x_i, y_j) \rangle, \quad (19)$$

where  $\langle \Sigma_{MHP}(x_i, y_j) \rangle$  is the mean surface density  $\Sigma_{MHP}$  inside the area of the squared pixel centered at  $(x_i, y_j)$ . We consider this component as a 3D exponential disc with vertical distribution given by (10). In order to obtain an expression similar to (6) for the disc in model C we work in the same way as in model B. Table 4 in Appendix gives the values of the amplitudes of  $\Phi_0(R_i)$ ,  $\Phi_{lc}(R_i)$ ,  $\Phi_{ks}(R_i)$  of the potential corresponding to the disc component.

Figure 7 shows the data of the observational rotational velocities (Lindblad et al. 1997) as in the two previous models together with the rotation curve of the luminous component (both MHP and disc) along the major axis of the bar represented by the dotted curve. Also in this case the activation of the two additional potential terms, especially the DH one, allows a better relation between the rotation curve of the model along its bars major axis and the inclination of the observed HI curve at large distances. The values of their parameters for model C are also shown in Table 1.

## 5 THE NONLINEARITY OF THE MODELS

As a measure of the nonlinearity of the models we consider the quantity

$$Q = \frac{|\Delta \mathbf{F}|}{|\mathbf{F}_{axis}|} = \frac{|\mathbf{F}_{total} - \mathbf{F}_{axis}|}{|\mathbf{F}_{axis}|} = \frac{\sqrt{\left(\frac{\partial \Phi_{total}}{\partial R} - \frac{\partial \Phi_{axis}}{\partial R}\right)^2 + \left(\frac{1}{R} \frac{\partial \Phi_{total}}{\partial \theta}\right)^2}}{\left|\frac{\partial \Phi_{axis}}{\partial R}\right|} \quad (20)$$

which is the ratio of the modulus of the vectorial difference of the total force (axisymmetric and non-axisymmetric) from the axisymmetric force, over the modulus of the axisymmetric force. Thus,  $Q$  measures the non-axisymmetric force perturbation, normalized over the axisymmetric one. This parameter describes well the non-linear effect of the non-axisymmetric components but it is unable to determine by itself the global dynamics in a rotating system (see below the discussion about the importance of  $\Omega_p$ ).

In the past, the strength of bars and spirals in disc galaxies has been quantified by means of similar indices (e.g. Buta & Block 2001; Vorobyov 2006). The index introduced by Buta & Block (2001) has been widely used in large samples of galaxies (Laurikainen & Salo 2002; Block et al. 2004; Laurikainen et al. 2004). This index is similar to the quantity  $Q$  defined in Eq. (20). The variation of  $Q$  in our models is presented in Fig. 8.

At the left-hand column the panels show in color diagrams the strength of the non-axisymmetric force, measured by  $Q$ , for the three models. Each model is indicated at the right edge of the figure. At the right-hand column we plot the maximum  $Q$  as a function of  $R$  (black solid curves). We observe that the overall maximum perturbation strength reaches higher values ( $\approx 0.8$ ) in model A (pure 2D), while in the other two models it is lower reaching  $\approx 0.45$  and  $\approx 0.5$  for models B and C respectively. The maximum  $Q$  values of models B and C are close to those presented by Laurikainen & Salo (2002), while the pure 2D case has a significant larger overall maximum  $Q$  value. In each panel of the right-hand column we have plotted additional maximum  $Q$  curves corresponding to different parameter values, which are indicated in the figure. The green curves give the maximum  $Q$  profiles without the DH component. We observe that the maximum  $Q$  values, with the DH component included, are approximately 0.8-0.85 of the corresponding values neglecting the DH component. Such values are within the range of values given by Buta et al. (2004), although towards the lower limit. We studied also the robustness of the maximum  $Q$  profile to the adopted orientation parameters. We considered two additional orientation parameter sets i.e. (PA, IA) = (106.6°, 42.2°) (dashed magenta curve, Fig. 8b) and (PA, IA) = (67°, 28°) (dashed blue curve, Fig. 8b). The first set of the orientation parameters is the one obtained from near-infrared data by Grosbøl et al. (2004). The second set has angles deviating from the values we finally used as much as the first one, but to the opposite direction. We observe, that the maximum  $Q$  value, in these cases, is affected by less than 10%. We also checked the dependence of the maximum  $Q$  value on the changes of the zero-value level, which yield to disc scale lengths of 7 kpc (dashed red curve, Fig. 8b) and 13 kpc (dashed-dotted orange curve, Fig. 8b), respectively. Note, that the exponential discs with these scale lengths do not fit the corresponding data as well as in the original  $h_R=10$  kpc case. We observe, that the maximum  $Q$  value, in these cases, is affected by less than 5%.

In Fig. 8d we see that the maximum  $Q$  value, in model B,



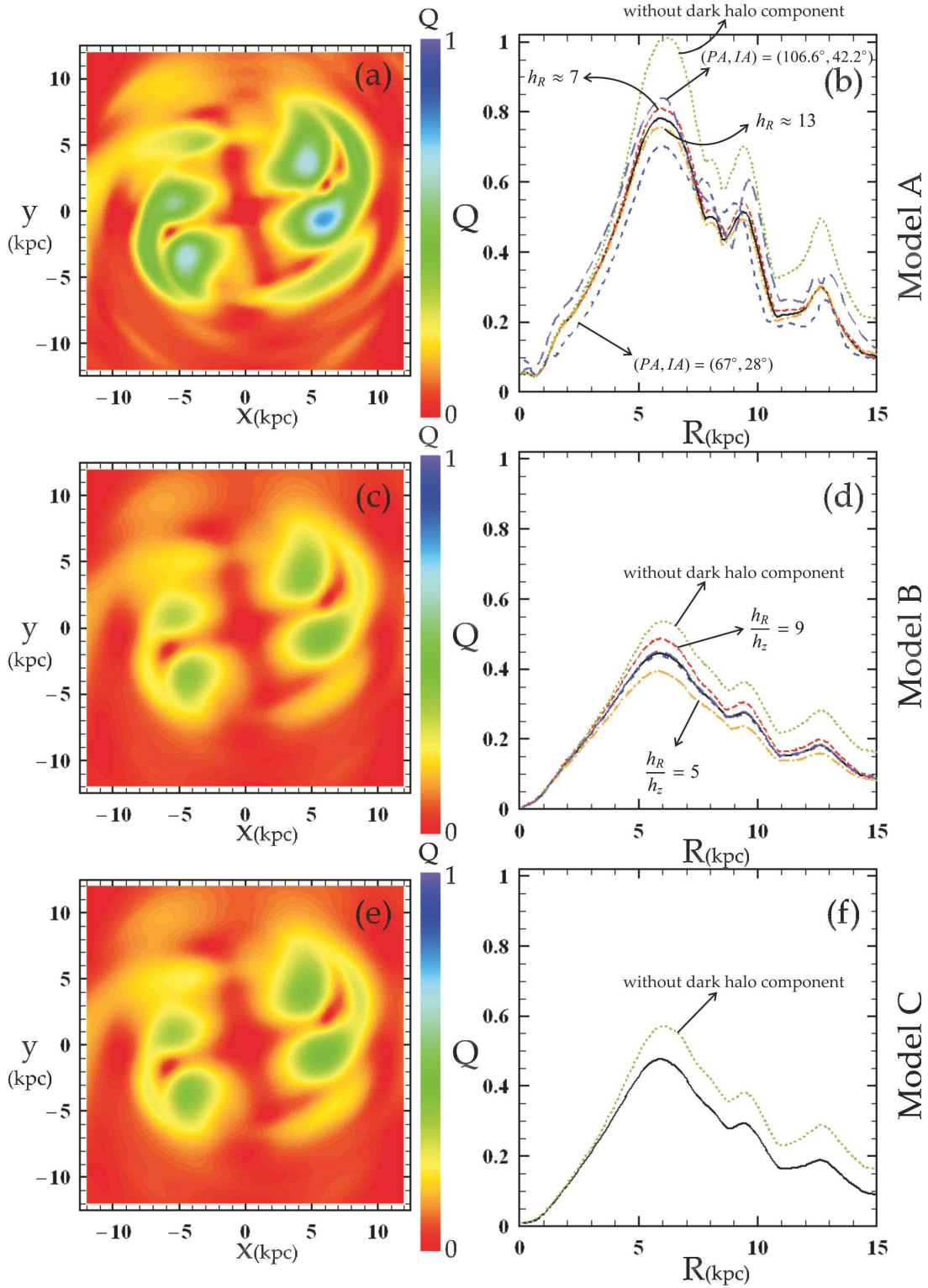


**Figure 8.** The  $Q$  variation in our three models for several sets of the potential parameters. The panels of the left-hand column give  $Q$  for models “A” (a), “B”(c) and “C”(e). The panels of the right-hand column give the maximum  $Q$  as a function of  $R$  (black solid curves). Additional curves refer to the radial variation of maximum  $Q$  in models with different parameters than those used in the basic set-up of the three general models. For model “A” in panel (b) the dotted green curve refers to a model without dark halo, the magenta and blue dashed curves to different orientation parameters, while the dashed pink and dark yellow ones to models with disc scale lengths  $h_R = 7$  kpc and  $h_R = 13$  kpc respectively. Arrows help to better trace each curve. For model “B” in panel (d), additional curves are given for a “model B” without dark halo component (dotted green curve) and models with  $h_R/h_z = 5, 9$ . Finally for model “C”, panel (f), an additional curve gives the radial variation of  $Q$  again in a model that with respect to “C” does not have any dark halo component.

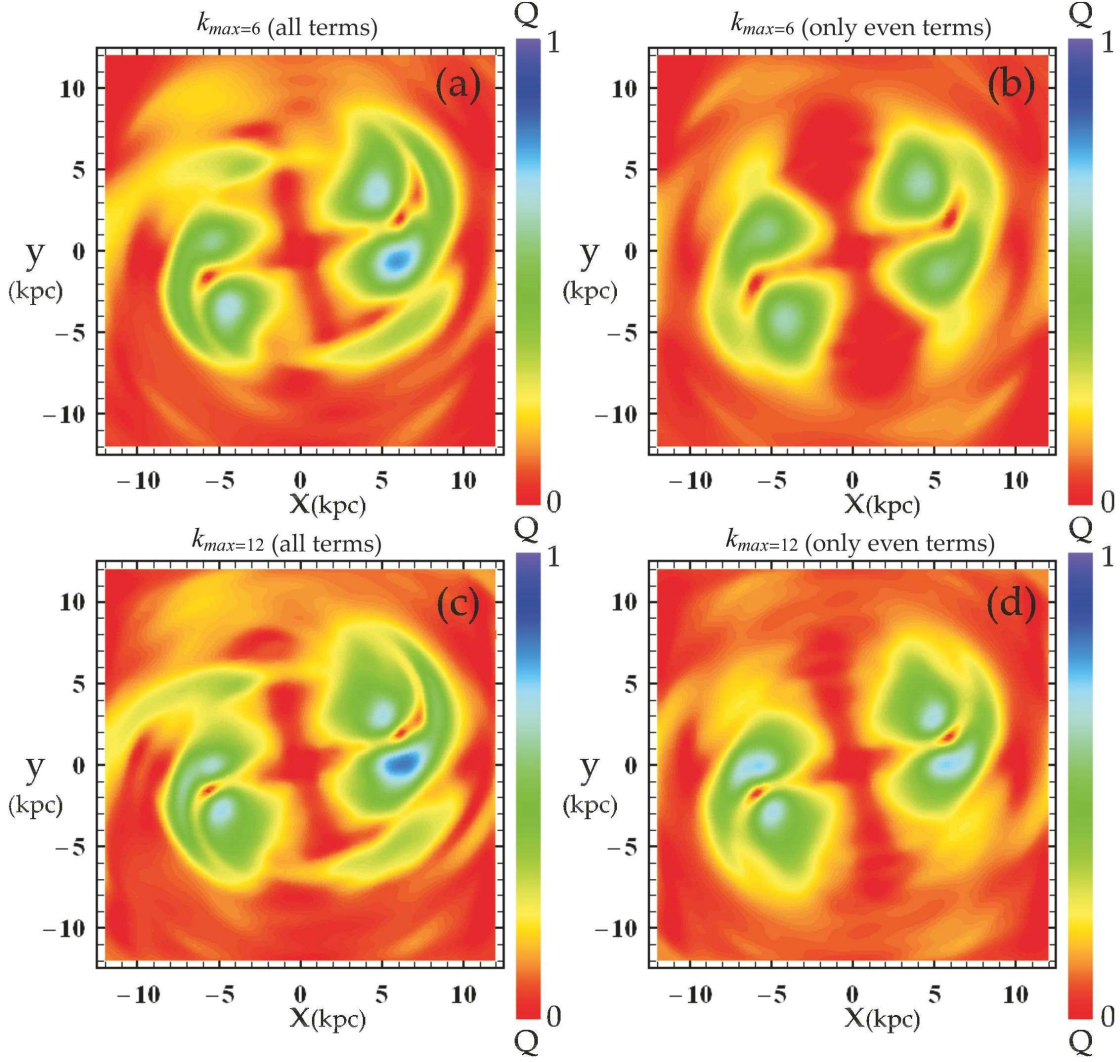


**Figure 9.** The  $Q$  value maps for model A on the galactic plane for  $k_{max} = 6$ ,  $k_{max} = 12$  (first and second row respectively) with and without odd terms (left-hand column and right hand column respectively). A combination that can be used for reliable dynamical models is with  $k_{max} = 6$ , including all terms (panel (a)).

varies approximately by 10% when the ratio  $h_R/h_z$  varies  $1\sigma$  from its mean value (see dashed-dotted orange and dotted red curves in Fig. 8d). We also certified, that the  $Q$  profiles almost coincide within  $1\sigma$  variation of the exponent  $n$  of Eq. (10) from its mean value.

Special attention has been given to the number and kind (even or odd) of the Fourier terms to be included in the potential. The morphological asymmetries observed in the galaxy underline the importance of the inclusion of the odd terms for dynamical studies. The number and the kind of the Fourier terms may affect the maximum  $Q$  value as well as the 2D distribution of the  $Q$  value on the galactic plane. In order to study these effects we constructed  $Q$  value maps on the galactic plane for different combinations of the Fourier terms (Fig. 9). We present the results for model A since it is the model with the highest non-axisymmetric amplitudes in the Fourier decomposition. The upper two panels (a,b) of Fig. 9 include terms up to  $k_{max} = 6$  in Eq. (6), while the two panels at the bottom (c,d) up to  $k_{max} = 12$ . The left panels (a,c) include *all*  $k$  terms, while the right ones (b,d) only the even terms, as indicated at the top of each of them. By including all terms, the maximum  $Q$  value

for the case we consider up to  $k_{max} = 6$  is 0.96 of the maximum value corresponding to  $k_{max} = 12$ . By including higher order terms ( $k_{max} > 12$ ), the maximum  $Q$  value does not get further refinement. On the other hand, by neglecting the odd terms, the  $Q$  map clearly fails to reproduce all the asymmetries and the maximum  $Q$  value becomes at least 10% lower than that with the odd terms even for the  $k_{max} = 12$  case. More specifically, the maximum  $Q$  values corresponding to panels (a), (b), (c) of Figure 9 are 0.96, 0.89, 0.84 of the maximum  $Q$  value we get in Fig. 9c. We can observe, that at the sides of the bar the prominent green "tails", which essentially describe the force field at the spirals' region, are conspicuous only in panels (a) and (c). Also at radii around 8 and 9 kpc, at the ends of the bar, only panels (a) and (c) give a rather constant green shade, while at the same radii green color fades out in panel (b), but also in (d). Evident is that in terms of nonlinearity of the potential the odd terms are essential, while including  $k > 6$  terms does not improve the models at a level worth the additional computing time needed for the calculations. Thus, a reliable combination that can be used in dynamical studies is  $k_{max} = 6$  with all even and odd terms included (Fig. 9a).

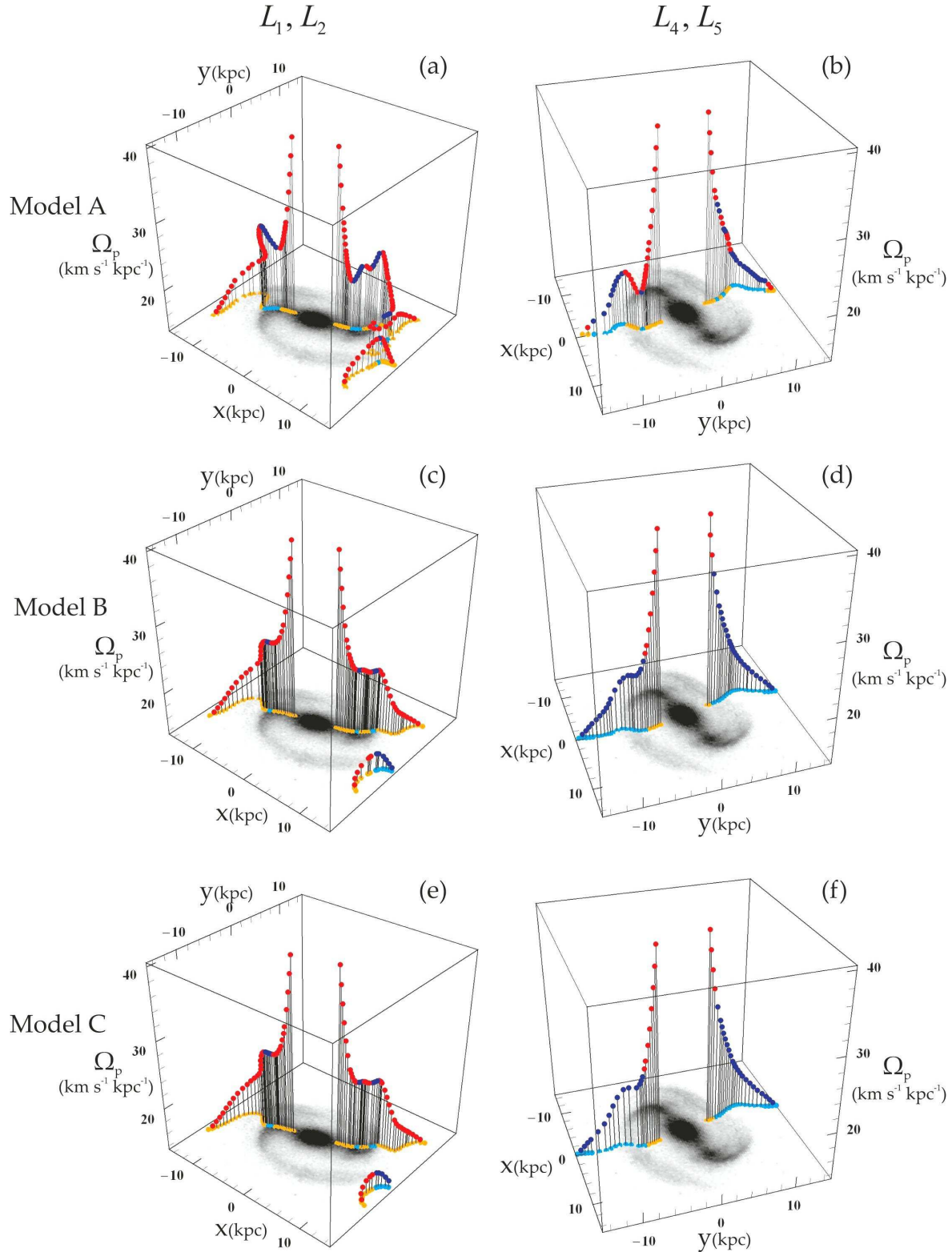


**Figure 10.** The loci of the Lagrangian points ( $L_1, L_2$  in the left-hand column and  $L_4, L_5$  in the right-hand column) for all the models as a function of the  $\Omega_p$ . The red (blue) points correspond to unstable (stable) Lagrangian points. In each panel we have projected the Lagrangian points on the galactic plane. We observe that in all models there are ranges of  $\Omega_p$  values for which we have multiple Lagrangian points. This property is more evident in model A, where we observe longer ranges of  $\Omega_p$  values corresponding to multiple Lagrangian points. Note that the separated group of points which are located at high  $x$  values (seen in all the left-hand column panels) correspond to multiple  $L_1$  Lagrangian points ordered near-parallel to the  $y$  axes and they refer to cases with low  $\Omega_p$  values.



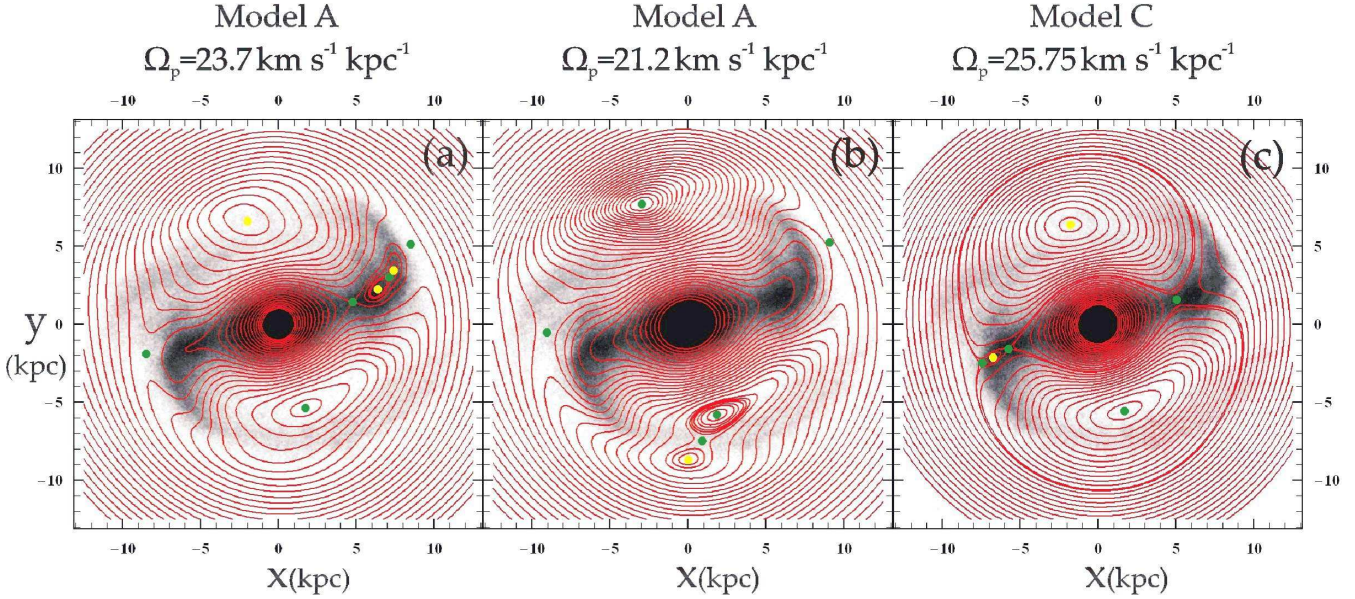


**Figure 11.** Some characteristic examples of multiple Lagrangian points. We plot the contour lines of the effective potential overlapped with the image of the galaxy for the cases and the  $\Omega_p$  values indicated in the figure. Big yellow (green) dots correspond to stable (unstable) Lagrangian points. In (a) we see 3 unstable and 2 stable  $L_1$  points. In (b) we have 2 stable and 1 unstable  $L_5$  points. In (c) finally we see 2 unstable and 1 stable  $L_2$  points. Note that the considered sense of rotation is clockwise.

In all examined cases the forcing of the models suggests that our systems are strongly nonlinear, since the perturbing term is at least higher than 40% of the axisymmetric background. This is a usual situation in models of strong barred galaxies (Kaufmann & Contopoulos 1996).

We note that potential evaluations for NGC 1300 have been previously done by England (1989), Hunter (1990), Lindblad & Kristen (1996), Aguerri et al. (2001) and more recently by Laurikainen & Salo (2002) using a 2MASS K-band image and by Laurikainen et al. (2004) by means of OSUBSG H-band data. These potentials have some features similar with our general model (for a discussion see Sect. 7). In our case, emphasis is given in constructing a potential function suitable for dynamical studies. We kept fixed the quantities that could be derived directly from our near-infrared K-band data, while the parameters that could be only confined within some range have been treated as free parameters. However, the most important parameter for the dynamics of a rotating disc galaxy is the pattern speed (for a review see Contopoulos 2004), which is an unknown quantity. The most simple assumption is that the system we are studying has a unique pattern speed. We take it as a basic hypothesis, the validity of which will be evaluated from the feedback we will get from response models (to be presented in subsequent papers). At any rate, it is the *effective potential* that determines the force field in our calculations. The dynamics of two systems with the same potential  $\Phi$  but with considerably different pattern speeds are considerably different (see e.g. Patsis et al. 1991). An investigation of the basic categories of effective potentials is presented in Sect. 6 below.

## 6 EFFECTIVE POTENTIALS

The locations of the stationary (stable and unstable) Lagrangian points strongly affect the dynamical properties of a rotating galaxy. The Lagrangian points and their stability structure the phase space

at the corotation region. Given a mass distribution, the positions of the Lagrangian points are determined by the value of the pattern speed  $\Omega_p$ . In the rotating frame we have the conservation of the Jacobi integral

$$E_j = \frac{1}{2}v^2 + \Phi_{eff}, \quad (21)$$

where  $\Phi_{eff}$  is the effective potential

$$\Phi_{eff}(x, y) = \Phi_T(x, y) - \frac{1}{2}\Omega_p^2(x^2 + y^2). \quad (22)$$

The stationary Lagrangian points at the equilibrium positions are defined by

$$\frac{\partial \Phi_{eff}(x, y)}{\partial x} = \frac{\partial \Phi_{eff}(x, y)}{\partial y} = 0. \quad (23)$$

This is the case of course, where the system rotates with a single pattern speed. In systems with multiple pattern speeds, multiple corotation radii will be defined on the disc. If bar and spirals rotate with different  $\Omega_p$ , each component will have its own corotation radius. In what follows we take the single pattern speed case as our initial assumption. Its validity and its limitation will be examined by means of models in subsequent papers.

Fig. 10 shows in a compact way how the number, the location and the stability of the Lagrangian points change on the disc for the various effective potentials. In Fig. 10a we give the positions  $(x, y)$  of the  $L_1, L_2$  Lagrangian points as a function of  $\Omega_p$  for model A. The calculation of the stability of the equilibrium points is done by following the standard procedure that can be found in relevant textbooks (see e.g. Binney & Tremaine 2008, pp. 179-183). The red and blue points correspond to the unstable and stable Lagrangian points, respectively. At the basis of the cubes in all panels it is plotted the surface density of the galaxy together with the projections of the corresponding Lagrangian points. The projected orange and light blue points correspond to the unstable and stable Lagrangian points, respectively. Figure 10b is similar to Fig. 10a and shows the

positions of  $L_4, L_5$  Lagrangian points in model A. We observe that there are ranges of  $\Omega_p$  values for which there are more than one  $L_1, L_2, L_5$  points. Figures 10c,d and 10e,f are similar to Fig. 10a,b but for the model B and C, respectively. We see that the distribution of Lagrangian points have a very similar behavior in models B and C. Moreover, the variability of the positions of the Lagrangian points with  $\Omega_p$  seems smoother in models B and C. However, even in these cases we have ranges of  $\Omega_p$  values corresponding to multiple Lagrangian points (see Fig. 11c).

Figure 11 presents some characteristic cases of effective potentials with multiple Lagrangian points. Stable (unstable) Lagrangian points are plotted with yellow (green) big dots. Fig. 11a shows the isocontours of the effective (total) potential, in model A, for  $\Omega_p = 23.7 \text{ km sec}^{-1} \text{ kpc}^{-1}$ . In this figure we observe 5  $L_1$  Lagrangian points (3 unstable and 2 stable) at the region close to the end of the bar. Figure 11b corresponds to the same model A but for  $\Omega_p = 21.2 \text{ km sec}^{-1} \text{ kpc}^{-1}$ . We observe 3  $L_5$  Lagrangian points (2 stable, 1 unstable). Finally, Fig. 11c corresponds to model C for  $\Omega_p = 25.75 \text{ km sec}^{-1} \text{ kpc}^{-1}$  and shows 3  $L_2$  Lagrangian points (2 unstable, 1 stable).

## 7 DISCUSSION AND CONCLUSIONS

In this paper, we propose three different general models for the potential of the grand design barred-spiral galaxy NGC 1300, based on observations in the near-infrared. The ultimate goal of our work is the investigation of the stellar dynamics of this galaxy by means of response models and orbital theory. More precisely we want to reveal the dynamical mechanisms that shape the observed structure of the galaxy. This is done in the forthcoming papers of this series.

Observations in the near-infrared provide the most reliable potential models of disc galaxies, since they are excellent indicators of the distribution of mass associated to stellar matter. The needed additional assumptions refer mainly to the distribution of luminous matter in the third dimension (outside the galactic plane) and to the distribution of the non-luminous matter (dark halo and central mass concentration).

The three proposed models are: The pure 2D case (Model A), where all luminous matter is considered on the galactic plane; the thick disc case (Model B) where all luminous matter is considered in a 3D disc with a constant scale height; and the ‘‘spheroidal case’’ (Model C) in which the major part of the bar is a spherical modified Hubble profile. The remaining luminous matter is attributed to a 3D disc as in Model B. In all these cases the calculation of the potential is performed by means of an FFT transform technique, that has been introduced in various versions by (Hohl & Hockney 1969; Quillen et al. 1994; Laurikainen & Salo 2002).

These three general models can be considered as limiting cases in the parameter space of models whose responses and orbital content will be studied. Let us consider an unknown parameter, e.g. the disc thickness. If we find that we obtain better feedback in Model A than in Model B, we will conclude that we have more accurate dynamics closer to the thin disc limit. Only the study of the dynamics in a large number of effective potentials will show which configuration compares best with the observed morphology.

As we have seen in Section 5, all models are strongly nonlinear. The relative force perturbation (regarding the axisymmetric background) in all models is high reaching to 45%-50% in Models B and C and to even higher value 80% in Model A. We note that *for normal (non-barred) spiral galaxies* the models that reproduce successfully the morphology of this type of galaxies have maximum

force perturbations typically of the order of 5-10% (Patsis et al. 1991; Laurikainen & Salo 2002; Laurikainen et al. 2004; Vorobyov 2006) and they are already characterized by nonlinear effects. Nonlinear effects are even stronger in larger perturbation characteristic of bars (see Kaufmann & Contopoulos 1996; Laurikainen & Salo 2002; Laurikainen et al. 2004; Block et al. 2004, and others). Thus, it is expected that all models will present a strongly nonlinear behavior with extended chaotic regions. Note that we certified the robustness of the force perturbation in each model to small changes of the various required parameter values (e.g. thickness of the disc).

The nonlinearity of a model, expressed as the relative force perturbation, is an important parameter for studying its dynamics, since it refers to the total distribution of matter (luminous and dark) in the galaxy. However, the estimation of the potential of a disc galaxy alone does not determine its dynamics. The main, and most important, parameter is the pattern speed and this cannot be unambiguously determined from observations. The Coriolis forces totally alter the landscape of the gravitational field, as we can see in the various effective potentials. A potential by itself can tell us whether or not nonlinear phenomena can play an important role in the dynamics of the system. However, for the same potential we can have totally different dynamics. By varying the pattern speed the equilibrium (Lagrangian) points are shifted and may alter their stability character. In our analysis we find cases with multiple Lagrangian points. This indicates that in real galaxies the existence of multiple Lagrangian points can be a common phenomenon. Our models give the opportunity to study the dynamics of such realistic systems, something that has not been done yet. The effect of the variation of the pattern speed on the dynamics of NGC 1300 will be presented in the forthcoming papers of this series.

## ACKNOWLEDGMENTS

We thank Prof. G. Contopoulos for fruitful discussions. P.A.P thanks ESO for a two-months stay in Garching as visitor, where part of this work has been completed. We would also like to thank the anonymous referee for constructive comments that helped the clarity and the presentation of our paper.

## REFERENCES

- Aguerre J., Prieto M., Varela A., Munoz-Tunon C., 2001, *Astroph. S. Sc.*, 276, 611
- Binney J., Tremaine S., 2008, *Galactic Dynamics*. Princeton University Press, New Jersey
- Block D., Buta R., Knapen J. e. a., 2004, *AJ*, 128, 183
- Buta R., Block D. L., 2001, *ApJ*, 550, 243
- Buta R., Laurikainen E., Salo H., 2004, *AJ*, 127, 279
- Contopoulos G., 2004, *Order and Chaos in Dynamical Astronomy*. Springer-Verlag, New York
- Contopoulos G., Patsis P. A., 2008, in Contopoulos G., Patsis P. A., eds, *Chaos in Astronomy Lecture Notes In Physics*. Springer-Verlag, Berlin
- de Grijs R., 1998, *MNRAS*, 299, 595
- de Vaucouleurs G., de Vaucouleurs A., Corwin H. G., Buta R., Paturel G., Fouque P., 1991, *Third Reference Catalogue of Bright Galaxies*, 363
- Elmegreen D. M., Elmegreen B. G., Chromey F. R., Hasselbacher D. A., 1996, *ApJ*, 469, 131
- England M. N., 1989, *ApJ*, 337, 191

- Fabbiano G., Gioia I. M., Trinchieri G., 1988, *ApJ*, 324, 749  
 Gaddoti D. A., 2008, *MNRAS*, 384, 420  
 Grosbøl P., 2008, in Contopoulos G., Patsis P. A., eds, *Chaos in Astronomy Lecture Notes In Physics*. Springer-Verlag, Berlin, p. 23  
 Grosbøl P., Dottori H., 2008, *A&A*, 490, 87  
 Grosbøl P., Patsis P. A., 1998, *A&A*, 336, 840  
 Grosbøl P., Patsis P. A., Pompei E., 2004, *A&A*, 423, 849  
 Hohl F., Hockney R. W., 1969, *J. Comput. Phys.*, 4, 306  
 Hunter J., 1990, *Ann.N.Y. Acad. Sci.*, 596, 174  
 Kaufmann D. E., Contopoulos G., 1996, *A&A*, 309, 381  
 Kregel M., van der Kruit P. C., de Grijs R., 2002, *MNRAS*, 334, 646  
 Laurikainen E., Salo H., 2002, *MNRAS*, 337, 1118  
 Laurikainen E., Salo H., Buta R., Vasylyev S., 2004, *MNRAS*, 355, 1251  
 Lindblad P., Kristen H., 1996, *A&A*, 313, 733  
 Lindblad P. A. B., Kristen H., Joersaeter S., Hoegbom J., 1997, *A&A*, 317, 36  
 Patsis P. A., Contopoulos G., Grosbol P., 1991, *A&A*, 243, 373  
 Patsis P. A., Héraudeau P., Grosbøl P., 2001, *A&A*, 370, 8  
 Prieto M., Aguerri J. A. L., Varela A. M., Muñoz-Tuñón C., 2001, *A&A*, 367, 405  
 Quillen A. C., Frogel J. A., Gonzalez R. A., 1994, *ApJ*, 437, 162  
 Rix H. W., Rieke M. J., 1993, *ApJ*, 418, 123  
 Seigar M. S., Block D. L., Puerari I., Chorney N. E., James P. A., 2005, *MNRAS*, 359, 1065  
 van der Kruit P. C., 1988, *A&A*, 192, 117  
 van der Kruit P. C., 2002, in Costa G. S. D., Jerjen H., eds, *The Dynamics, Structure & History of Galaxies Vol. 273 of ASP Conference Proceedings*. Astronomical Society of the Pacific, San Francisco, p. 7  
 Vorobyov E. I., 2006, *MNRAS*, 370, 1046